PHYSICAL REVIEW B **85**, 035414 (2012)

Functional renormalization group and variational Monte Carlo studies of the electronic instabilities in graphene near $\frac{1}{4}$ doping

Wan-Sheng Wang,[1] Yuan-Yuan Xiang,[1] Qiang-Hua Wang,[1] Fa Wang,[2] Fan Yang,[3] and Dung-Hai Lee[4,5]

[1]*National Lab of Solid State Microstructures, Nanjing University, Nanjing 210093, China*

[2]*Department of Physics, Massachusetts Institute of Technology, Cambridge, Massachusetts 02139, USA*

[3]*Department of Physics, Beijing Institute of Technology, Beijing 100081, China*

[4]*Department of Physics, University of California at Berkeley, Berkeley, California 94720, USA*

[5]*Materials Sciences Division, Lawrence Berkeley National Laboratory, Berkeley, California 94720, USA*

(Received 27 September 2011; revised manuscript received 30 November 2011; published 9 January 2012)

We study the electronic instabilities of near 1/4 electron doped graphene using the singular-mode functional renormalization group, with a self-adaptive k mesh to improve the treatment of the van Hove singularities, and variational Monte Carlo method. At 1/4 doping the system is a chiral spin-density wave state exhibiting the anomalous quantized Hall effect. When the doping deviates from 1/4, the $d_{x^2-y^2}+id_{xy}$ Cooper pairing becomes the leading instability. Our results suggest that near 1/4 electron or hole doping (away from the neutral point) the graphene is either a Chern insulator or a topoligical superconductor.

DOI: 10.1103/PhysRevB.85.035414 PACS number(s): 71.27.+a, 81.05.ue, 74.20.Rp, 74.70.Wz

I. INTRODUCTION

Graphene, a single atomic layer of graphite, has been a focus of interest since the pioneering work of Novoselov and Geim.[1] At the fundamental level the past research activities on graphene mostly focused on exploring the consequences of the unique Dirac-like band structure.[2] On the experimental side, few exceptions include the observation of the fractional quantum Hall effect,[3,4] the detection of the Fermi velocity renormalization,[5] and the possible observation of "plasmaron" in angle-resovled photosemission.[6] In general the effects of electron-electron interaction on the properties of graphene remain a frontier of this field. Previously based on the resonating-valence-bond[7] concept Pathak *et al.*[8] and Black-Schaffer and Doniach[9] proposed that doped graphene should be a high-temperature superconductor with $d+id'$ pairing symmetry. (Henceforth d and d' are used to denote interchangeably $d_{x^2-y^2}$ and d_{xy} symmetries, respectively.) In particular, the possibility of unusual superconductivity and other orders in doped graphene with van Hove singularities at (or near) the Fermi level becomes a hot issue.[10,11] Most recently by a perturbative renormalization group calculation Nandkishore *et al.* concluded that the van Hove singularities on the Fermi surface drive chiral $d+id'$ superconductivity in the limit of vanishing interaction strength.[12]

On a different front, Li recently proposed that due to the existence of Fermi-surface nesting the 1/4 electron doped Hubbard model on honeycomb lattice favors the formation of a magnetic insulating state, which possesses nonzero spin chirality and exhibits the anomalous quantized Hall effect, hence is a Chern insulator.[13] Thus near quarter doping graphene suddenly becomes a playing ground where either a Chern insulator or a topological superconductor can potentially be realized. Because the realization of either phase in heavily doped graphene will be truly exciting, we feel it is meaningful to examine this problem using the more realistic band structure and interaction parameters.

In view of the heavy doping we use the Hubbard interaction to model the screened Coulomb interaction. We perform singular-mode functional renormalization group (SM-FRG)[14] and variational Monte Carlo (VMC) calculations to address the possible electronic instabilities. Since the interaction strength is estimated to be a fraction of the bandwidth, we believe SM-FRG should yield the qualitatively correct answer. The VMC is used to further confirm such a belief. The main results are summarized as follows. At 1/4 electron doping and for interaction strength appropriate for graphene we found that the chiral spin density wave (SDW) state is the dominating instability. When the doping level slightly deviates from 1/4 we find that the $d+id'$ pairing instability surpasses that of the chiral SDW. We propose a schematic phase diagram in Fig. 6(b). As in pnictides and overdoped cuprates,[15] the pairing mechanism is due to a strong scattering channel shared by the SDW and pairing.

II. MODEL

The real-space Hamiltonian we used is given by

$$H=-\sum_{(ij)\sigma}(c^{\dagger}_{i\sigma}t_{ij}c_{j\sigma}+\text{H.c.})-\mu N_e+U\sum_i n_{i\uparrow}n_{i\downarrow}+\frac{1}{2}V\sum_{i\delta}n_i n_{i+\delta}, \quad (1)$$

where (ij) denotes bonds connecting sites i and j, σ is the spin polarity, μ is the chemical potential, N_e is the total electron number operator, the U term is the on-site Hubbard interaction, and V is the Coulomb interaction on nearest-neighbor bonds δ. The honeycomb lattice has two sublattices, which we denote as A and B henceforth. As suggested in Ref. 2 we take $t_1=2.8$ eV, $t_2=0.1$ eV, and $t_3=0.07$ eV for hoppings between the first, second, and third neighbors, respectively, and set $U=3.6t_1$. As for V, we expect $V<U$ in doped graphene, and take $V=t_1$ as a typical upper bound. Theoretically, enriched phases may appear for even larger values of V/U.[11,16]

III. METHOD

The SM-FRG method[14] we used is a modification of the FRG method[17] applied to the cuprates[18] and pnictides.[19]

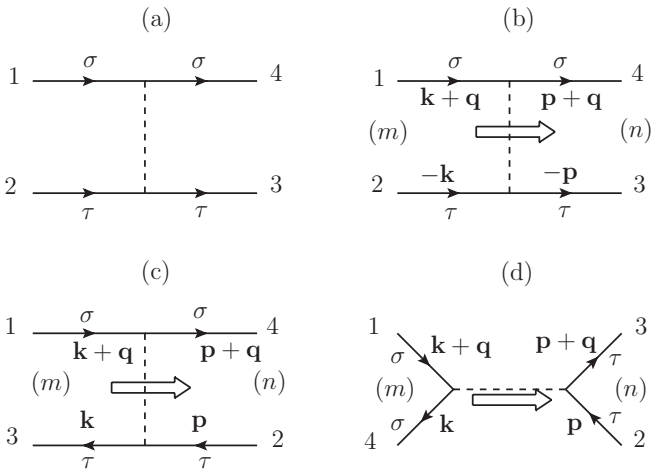

FIG. 1. A generic 4-point vertex (a) is rearranged into the pairing (b), crossing (c) and direct (d) channels. Here $\mathbf{k},\mathbf{q},\mathbf{p}$ are momenta, σ and τ denote spins which are conserved during fermion propagation, and m,n denote the form factor (see the text for details). The open arrows indicate collective propagation.

Figure 1(a) shows a generic four-point vertex function Γ_{1234}, which appears in the interaction $c_1^\dagger c_2^\dagger(-\Gamma_{1234})c_3 c_4$. Here 1,2,3,4 represent momentum (or real-space position) and sublattice. The spin σ and τ are conserved during fermion propagation, and will be suppressed henceforth. Figures 1(b)–1(d) are rearrangements of (a) into the pairing (P), the crossing (C), and the direct (D) channels in such a way that a collective momentum $\mathbf{q}$ can be associated and the other momentum dependence can be decomposed as

$$\begin{aligned}\Gamma_{\mathbf{k+q},-\mathbf{k},-\mathbf{p},\mathbf{p+q}} &\to \sum_{mn} f_m^*(\mathbf{k})P_{mn}(\mathbf{q})f_n(\mathbf{p}),\\ \Gamma_{\mathbf{k+q},\mathbf{p},\mathbf{k},\mathbf{p+q}} &\to \sum_{mn} f_m^*(\mathbf{k})C_{mn}(\mathbf{q})f_n(\mathbf{p}),\\ \Gamma_{\mathbf{k+q},\mathbf{p},\mathbf{p+q},\mathbf{k}} &\to \sum_{mn} f_m^*(\mathbf{k})D_{mn}(\mathbf{q})f_n(\mathbf{p}).\end{aligned} \tag{2}$$

Here $\{f_m\}$ is a set of orthonormal lattice form factors. For honeycomb lattice the form factor label m also includes a sublattice label, $m=(m,a)$ with $a=A/B$, within our choice of C_{3v} point group with respect to the atomic site (see the Appendix.) The decomposition into each channel would be exact if the set is complete. In practice, however, a set of a few form factors is often sufficient to capture the symmetry of the order parameters associated with leading instabilities.[14] The momentum space form factors are the Fourier transform of the real-space ones: (1) on site, $f_{s_0}(\mathbf{r})=1$; (2) first neighbor bonds, $f_{s_1}(\mathbf{r})=\sqrt{1/3}$, $f_{d_1}(\mathbf{r})=\sqrt{2/3}\cos(l\theta_\mathbf{r})$, and $f_{d_{1'}}(\mathbf{r})=\sqrt{2/3}\sin(l\theta_\mathbf{r})$, where $l=2$ and $\theta_\mathbf{r}$ is the azimuthal angle of $\mathbf{r}$;[20] (3) second neighbor bonds, $f_{s_2}(\mathbf{r})=\sqrt{1/6}$, $f_{p_2}=\sqrt{1/3}\cos\theta_\mathbf{r}$, $f_{p_{2'}}(\mathbf{r})=\sqrt{1/3}\sin\theta_\mathbf{r}$, $f_{d_2}(\mathbf{r})=\sqrt{1/3}\cos 2\theta_\mathbf{r}$, $f_{d_{2'}}(\mathbf{r})=\sqrt{1/3}\sin 2\theta_\mathbf{r}$, $f_{f_2}(\mathbf{r})=\sqrt{1/6}\cos 3\theta_\mathbf{r}$. These form factors (combined with sublattice labels) are used in all channels on equal footing. We have tested that further neighbor form factors do not change the results qualitatively.

The one-loop correction to the flow of the vertex function can be written as, in matrix form,

$$\begin{aligned}\partial P/\partial\Lambda &= P\chi'_{pp}P,\\ \partial C/\partial\Lambda &= C\chi'_{ph}C,\\ \partial D/\partial\Lambda &= (C-D)\chi'_{ph}D + D\chi'_{ph}(C-D),\end{aligned} \tag{3}$$

where the collective momentum $\mathbf{q}$ is left implicit for brevity, $\chi'_{pp/ph}$ are loop integrations projected by the form factors (see the Appendix for details), and Λ is the running cutoff energy. Integrating Eq. (3) with respect to Λ yields the ladder approximation. However, since ∂P, ∂C, and ∂D add up to the full change $d\Gamma$, the full flow equations for P, C, and D should be given by

$$\begin{aligned}dP/d\Lambda &= \partial P/\partial\Lambda + \hat{P}(\partial C/\partial\Lambda + \partial D/\partial\Lambda),\\ dC/d\Lambda &= \partial C/\partial\Lambda + \hat{C}(\partial P/\partial\Lambda + \partial D/\partial\Lambda),\\ dD/d\Lambda &= \partial D/\partial\Lambda + \hat{D}(\partial P/\partial\Lambda + \partial C/\partial\Lambda),\end{aligned} \tag{4}$$

where the $\hat{P}$, $\hat{C}$, and $\hat{D}$ are the projection operators in the sense of Eq. (2), and we used the fact that $\hat{K}(\partial K)=\partial K$ for $K=P,C,D$. In Eq. (4) the terms preceded by the projection operators represent the overlaps of the three different channels. It is those terms that allow pairing to be induced by virtual particle-hole scattering processes.[15]

It can be shown that the effective interaction in the superconducting (SC), spin-density wave (SDW), and charge-density wave (CDW) channels are given by $V_{sc}=-P$, $V_{sdw}=C$, and $V_{cdw}=C-2D$, respectively. By singular value decomposition, we determine the leading instability in each channel,

$$V_X^{mn}(\mathbf{q}_X)=\sum_\alpha S_X^\alpha\phi_X^\alpha(m)\psi_X^\alpha(n), \tag{5}$$

where $X=sc,sdw,cdw$, S_X^α is the singular value of the αth singular mode, ϕ_X^α and ψ_X^α are the right and left eigenvectors of V_X, respectively. We fix the phase of the eigenvectors by requiring $\mathrm{Re}[\sum_m \phi_X^\alpha(m)\psi_X^\alpha(m)]>0$ so that $S_X^\alpha<0$ corresponds to an attractive mode in the X channel. In the pairing channel $\mathbf{q}_{sc}=0$ addresses the Cooper instability. The pairing function in the sublattice basis can be constructed from ϕ_{sc}^α, and a further unitary transform is needed to get the pairing function in the band basis. (See the Appendix for details.) The ordering wave vector in the SDW/CDW channel $\mathbf{q}=\mathbf{q}_{sdw/cdw}$ is chosen at which $|V_{sdw/cdw}(\mathbf{q})|$ is maximal. We note that such a vector has symmetry-related images, and may change during the FRG flow before settling down to fixed values. The RG flow is stopped if any of $|P|_{\max}$, $|C|_{\max}$, or $|D|_{\max}$ becomes roughly ten times of the bandwidth.[21] More technical details can be found in the Appendix.

IV. RESULTS AND DISCUSSION

We define the doping level by $\delta=n_e-1$ where n_e is the number of electrons per site. We first discuss the results for $\delta=1/4$ and $V=0$. Figure 2(a) shows the Fermi surface in this case, which is well nested and close to the van Hove singularities (the midpoints of edges of the outer hexagon). The flow of the most negative singular values (denoted as S) in the SC, SDW, and CDW channels are shown in Fig. 2(b). Clearly

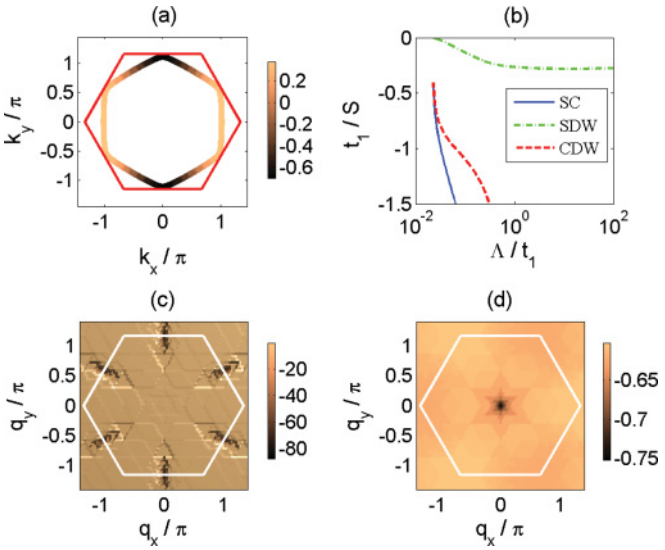

FIG. 2. (Color online) Results for $\delta = 1/4$ and $V = 0$. (a) The Fermi surface. The brightness on the surface represents the momentum space gap function associated with one of the degenerate pairing modes. (b) FRG flow of (the inverse of) the most negative singular values S in the SC (blue solid line), SDW (green dot-dashed line), and CDW (red dashed line) channels. (c) and (d) are the renormalized interaction V_{sdw}^{mm} for $m = (s_0, A)$, and V_{sc}^{mm} for $m = (d_1, A)$, as functions of the collective momentum $\mathbf{q}$. The hexagons in (a), (c), and (d) indicate the Brillouin-zone boundary.

the SDW (green dot-dashed line) is the leading instability. This is because the SDW scattering is already attractive at high energies and is further enhanced by the Fermi-surface nesting shown in Fig. 2(a) down to the lowest energies. This SDW singular mode $\phi_{sdw}(m)$ has a dominant value for $m = (s_0, A/B)$, showing that the magnetic ordering moment is site local. It is also identifiable in the renormalized interaction $V_{sdw}^{mm}(\mathbf{q})$ for $m = (s_0, A)$ shown in Fig. 2(c), which has strong peaks at three independent momenta $\mathbf{Q}_1 = (0, 2\pi/\sqrt{3})$, $\mathbf{Q}_2 = (-\pi, \pi/\sqrt{3})$, $\mathbf{Q}_3 = (\pi, \pi/\sqrt{3})$, and their symmetric images. They define the possible ordering vectors $\mathbf{q}_{sdw}$ for the SDW order. In contrast, the scattering associated with pairing (blue solid line) is initially repulsive in all channels, and only becomes attractive in the d-wave channel after the SDW scattering grows strong. Regarding Cooper pairing we find two degenerate leading form factors: the $d_{x^2-y^2}$ and d_{xy} doublets. One of these is used to generate the momentum space gap function shown in Fig. 2(a). The singular pairing mode $\phi_{sc}(m)$ is nonzero for the second neighbor bonds, but the amplitude is about one order of magnitude smaller than that for the first neighbor bonds, hence justifying the cutoff in the real-space range of the form factors. The renormalized $V_{sc}^{mm}(\mathbf{q})$ for $m = (d_1, A)$ in Fig. 2(d) has negative (but weak) peaks at $\mathbf{q} = 0$, confirming the Cooper instability at this momentum. The CDW channel (red dashed line) also becomes weakly attractive from Fig. 2(b). We checked that the singular mode $\phi_{cdw}(m)$ has significant values for $m = (s_1, A/B)$ and $m = (d_{1,1'}, A/B)$, showing that it is an extended CDW. The mixture of s_1 and $d_{1,1'}$ is due to the fact that the CDW wave vector $\mathbf{q} = (2\pi/3, \pi)$ (or its symmetry images) is not invariant

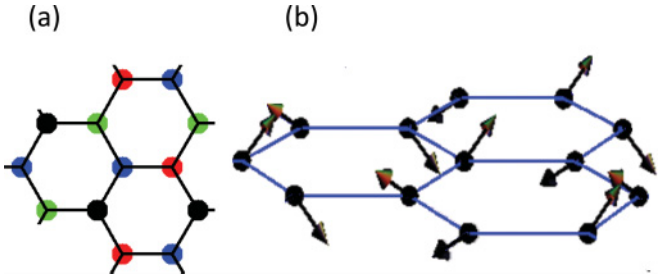

FIG. 3. (Color online) Chiral SDW order on the honeycomb lattice. (a) The spins on the black, red, green, and blue sublattices (of different gray scales) are $\mathbf{M}_1 + \mathbf{M}_2 + \mathbf{M}_3$, $-\mathbf{M}_1 - \mathbf{M}_2 + \mathbf{M}_3$, $\mathbf{M}_1 - \mathbf{M}_2 - \mathbf{M}_3$, $-\mathbf{M}_1 + \mathbf{M}_2 - \mathbf{M}_3$ respectively. (b) A three-dimensional perspective view of the chiral SDW order.

under the point-group operations. However, the CDW channel remains weak in our case hence will not be discussed in the rest of the paper. [The merging of SC and CDW lines in Fig. 2(b) is induced by the diverging SDW channel via the overlapping among these channels.]

The above results indicate three independent and degenerate SDW momenta (apart from the global spin SU(2) symmetry). A calculation that keeps the symmetry-breaking self-energy flow is needed to decide which combination of them is realized in the ordered state, but this is beyond the scope of the present work. Alternatively, one may resort to a Landau theory or mean-field theory. Indeed, according to the mean-field theory of Ref. 13, a particular linear combination,[13] $\langle \mathbf{S}_{\mathbf{R},A} \rangle = \mathbf{M}_3 e^{i\mathbf{Q}_3\cdot\mathbf{R}} + \mathbf{M}_1 e^{i\mathbf{Q}_1\cdot\mathbf{R}} + \mathbf{M}_2 e^{i\mathbf{Q}_2\cdot\mathbf{R}}$ and $\langle \mathbf{S}_{\mathbf{R},B} \rangle = \mathbf{M}_3 e^{i\mathbf{Q}_3\cdot\mathbf{R}} - \mathbf{M}_1 e^{i\mathbf{Q}_1\cdot\mathbf{R}} - \mathbf{M}_2 e^{i\mathbf{Q}_2\cdot\mathbf{R}}$, gives the most energetically favorable spin structure. Here $\mathbf{R}$ labels the unit cell and $\mathbf{M}_{1,2,3}$ are three mutually orthogonal and equal length vectors. The handedness of the $\mathbf{M}_{1,2,3}$ triad breaks time-reversal and spatial reflection symmetry. The resulting four-sublattice chiral SDW order is shown in Fig. 3.

Since our result is at odds with that of Ref. 12, which applies in the limit of vanishing interaction strength, we further check the above conclusion by a variational Monte Carlo (VMC) calculation using exactly the same parameters as for Fig. 2. We adopted the partially projected mean-field wave functions[22] as our trial wave functions, with the the form factors guided by the present SM-FRG result. Figure 4 shows the energy gain per site due to $d + id'$ pairing on 12×12 (circles) and 18×18 (triangles) lattices, showing negligible size dependence. We then compare to the energy gain associated with the chiral SDW (squares). It is clear that the SDW state is far more energetically favorable than the chiral $d + id'$-SC state at this doping level. The reason that the SDW state is realized in our lattice model lies in the fact that the perfect Fermi-surface nesting is as important as the intersaddle scattering addressed in Ref. 12.

Below 1/4 doping, the the Fermi level moves away from the van Hove points and the Fermi-surface nesting worsens. This is shown in Fig. 5(a) for $\delta = 0.211$ as an example. The bare interactions are still set as $U = 3.6t_1$ and $V = 0$. The SDW scattering is still attractive at high energies. As seen in Eq. (4), this relatively strong SDW channel causes attraction in the SC channel via overlap between these channels [terms with the projection operator in Eq. (4)]. At even lower energy scales

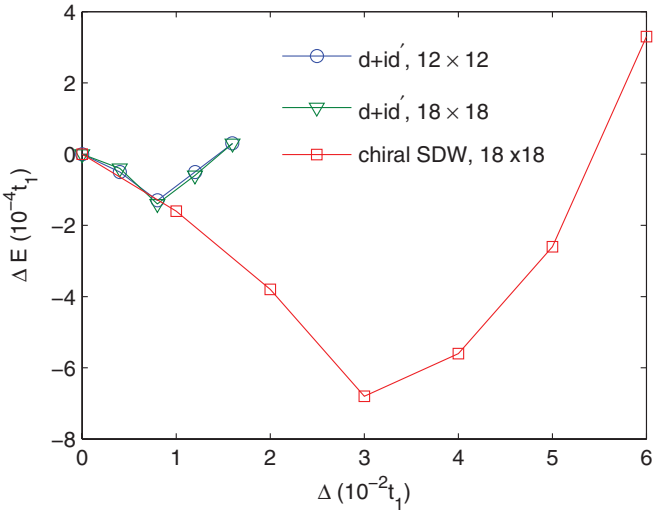

FIG. 4. (Color online) Variational Monte Carlo results for the energy gain per site, ΔE, versus the variational order parameters Δ for the $d + id'$-SC (circles and triangles) and the chiral SDW states (squares) at the doping level $\delta = 1/4$. The lattice sizes are given in the legends. Lines are guides to the eye.

the pairing channel attraction (with $\mathbf{q} = 0$) continues to grow due to the Cooper instability, while the enhancement of the SDW scattering is saturated due to the lack of Fermi-surface nesting. As a result the pairing instability surpasses the SDW instability at the lowest energy scale. This is shown by the flow of the singular values in Fig. 5(b). It is worthwhile to mention that precisely the same phenomenon was observed in the FRG studies of the cuprates and pnictides.[15,18] A close inspection of the eigenvectors $\phi_{sc}(m)$ associated with the most diverging superconducting pairing channel again finds the degenerate $d_{x^2-y^2}$ and d_{xy} doublets, with dominant amplitudes for $m = (d_{1,1'}, A/B)$. The momentum space gap function of

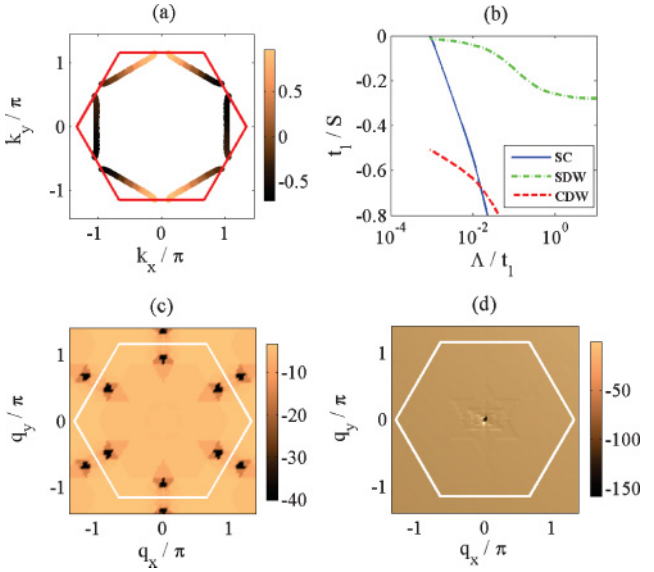

FIG. 5. (Color online) The same plots as in Fig. 2 but for $\delta = 0.211$. Note the splitting of the SDW peaks in panel (c) signifies the incommensurate SDW instability.

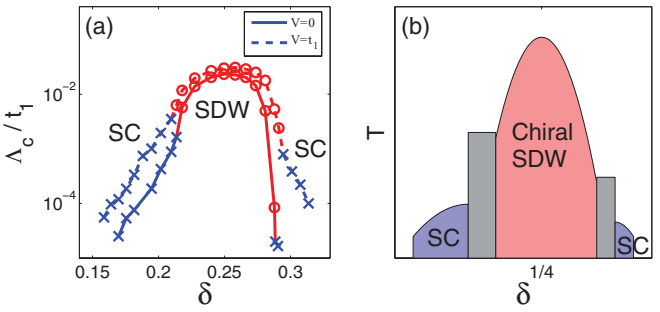

FIG. 6. (Color online) (a) The FRG diverging energy scale Λ_c plotted as a function of doping level near $\delta = 1/4$. Crosses and open circles represent Λ_c associated with the SC and SDW channel, respectively. $V = 0, t_1$ for solid and dashed lines, respectively. (b) A schematic temperature-doping phase diagram near $\delta = 1/4$ in linear scales. The gray region denotes the transition between SC and SDW.

one of the pairing modes is shown in Fig. 5(a). Figure 5(c) shows the renormalized $V^{mm}_{sdw}(\mathbf{q})$ for $m = (s_0, A)$, which shows weak peaks at six independent and incommensurate momenta. Figure 5(d) shows the renormalized $V^{mm}_{sc}(\mathbf{q})$ for $m = (d_1, A)$, which shows a strong negative peak at $\mathbf{q} = 0$.

We have also checked nearby doping and analyzed the competition between the incommensurate SDW and the SC state. In Fig. 6(a) we plot the higher diverging scale among these two competing orders as a function of doping (solid line). We found a similar phase diagram near $-1/4$ (hole) doping (not shown), mirroring that of electron doping. (Notice that the particle-hole symmetry is not exact in the presence of hopping integrals $t_{2,3}$.) The above results imply degenerate d-wave pairing instabilities. As for the degenerate SDW instabilities, additional analysis, such as the mean-field theory or Ginzburg-Landau theory, is needed to fix the structure of the pairing function in the ordered state. To a large extent, this kind of analysis has been performed in Ref. 12. We have also performed simple mean-field calculations using the renormalized pairing interaction. The result is that a time-reversal breaking $d_{x^2-y^2} \pm id_{xy}$-wave pairing is always more favorable. This could have been anticipated since both $d_{x^2-y^2}$ and d_{xy} form factors have nodes on the Fermi surface; a natural way to gain energy is to form the above chiral d-wave pairing, which gaps out the entire Fermi surface.

We now discuss briefly the effect of the nearest-neighbor interaction V. As a typical example, we set $U = 3.6t_1$ and $V = t_1$, and perform the FRG calculations. We find that the results are qualitatively similar to the cases with $V = 0$, except that in the leading pairing singular mode, $\phi_{sc}(d_{2,2'}, A/B)$ becomes slightly stronger, but still smaller than $\phi_{sc}(d_{1,1'}, A/B)$ by a factor of 4–6. The phase diagram for $V = t_1$ is also drawn in Fig. 6(a) (dashed line). The critical scale is slightly higher than in the case of $V = 0$. In the SC region this is due to the slight enhancement of d-wave pairing on second neighbor bonds. Unlike that claimed in Ref. 23, in all cases studied in this paper the f-wave pairing is not a leading instability.

We end by presenting Fig. 6(b) as a schematic phase diagram in the temperature-doping plane. In reality when the doping level slightly deviates from 1/4, the extra charges will be localized by the presence of disorder, which enables the

system to stay in the Chern insulator state for a finite doping interval. In the transition region marked by gray, where the doped charges delocalize, incommensurate SDW states with wave vectors shown in Fig. 5(c) will emerge.

V. SUMMARY

In summary, we have performed SM-FRG calculations for parameters suitable for graphene. Our results indicate that near 1/4 electron or hole doping, graphene is either a Chern insulator or a chiral d-wave superconductor. Both phases are topological in nature, and deserve experimental efforts in researching them.

ACKNOWLEDGMENTS

We thank Hong Yao for helpful discussions, and are grateful to Tao Xiang for computing resources. Q.H.W. acknowledges the support by NSFC (under Grants No. 10974086 and No. 10734120) and the Ministry of Science and Technology of China (under Grants No. 2011CBA00108 and No. 2011CB922101). F.Y. acknowledges the support by NSFC (under Grant No. 10704008). D.H.L. acknowledges the support by DOE Grant No. DE-AC02-05CH11231.

APPENDIX

To illustrate the idea of the method, we first ignore the sublattice index, and return to it at a later stage. The one-loop contributions to the flow of the irreducible four-point vertex function is shown in Fig. 7, where (a) and (b) lead to the flow of P and C, respectively, and (c)–(e) lead to the flow of D. The internal Green's functions are convoluted with the form factors, hence

$$
\begin{aligned}
(\chi'_{pp})_{mn} &= \frac{\partial}{\partial\Lambda}\int\frac{d\omega_n}{2\pi}\int\frac{d^2\mathbf{p}}{S_{BZ}} f_m(\mathbf{p})G(\mathbf{p}+\mathbf{q},i\omega_n) \\
&\quad\times G(-\mathbf{p},-i\omega_n)f_n^*(\mathbf{p})\theta(|\omega_n|-\Lambda) \\
&= -\frac{1}{2\pi}\int\frac{d^2\mathbf{p}}{S_{BZ}} f_m(\mathbf{p})G(\mathbf{p}+\mathbf{q},i\Lambda) \\
&\quad\times G(-\mathbf{p},-i\Lambda)f_n^*(\mathbf{p}) \quad +(\Lambda\to-\Lambda), \\
(\chi'_{ph})_{mn} &= \frac{\partial}{\partial\Lambda}\int\frac{d\omega_n}{2\pi}\int\frac{d^2\mathbf{p}}{S_{BZ}} f_m(\mathbf{p})G(\mathbf{p}+\mathbf{q},i\omega_n) \\
&\quad\times G(\mathbf{p},i\omega_n)f_n^*(\mathbf{p})\theta(|\omega_n|-\Lambda) \\
&= -\frac{1}{2\pi}\int\frac{d^2\mathbf{p}}{S_{BZ}} f_m(\mathbf{p})G(\mathbf{p}+\mathbf{q},i\Lambda) \\
&\quad\times G(\mathbf{p},i\Lambda)f_n^*(\mathbf{p}) \quad +(\Lambda\to-\Lambda),
\end{aligned}
\tag{A1}
$$

where G is the bare fermion propagator, S_{BZ} is the area of the Brillouin zone. Here $\Lambda > 0$ is the infrared cutoff of the Matsubara frequency ω_n.[24] As in usual FRG implementation, the self-energy correction and frequency dependence of the vertex function are ignored.

In general, the form factor $f_m(\mathbf{k}) = \sum_{\mathbf{r}} f_m(\mathbf{r})\exp(-i\mathbf{k}\cdot\mathbf{r})$, where $f_m(\mathbf{r})$ transforms according to an irreducible representation of the point group, and $\mathbf{r}$ is the relative position vector between the two fermion fields on each side of the diagrams in Figs. 1(b) and 1(c). For two types of diagrams to overlap, all of the four fermion fields sit within the range set by the form factors. Hence the projections in Eq. (4) are all preformed in real space.

We now return to the honeycomb lattice with two sublattices. The necessary modifications are as follows: (1) The sublattice label can be absorbed into the labels 1,2,3,4 in Figs. 1, so in principle the label m in the form factor $f_m(\mathbf{r})$ also includes sublattice indices. However, once $\mathbf{r}$ is fixed they are not independent.We absorb an independent index into the form factor label, $m \to (m,a)$, where a labels fermion field 1 or 4 in Fig. 1(b), 1 or 4 in Fig. 1(c), and 1 or 3 in Fig. 1(d). This is reasonable because the point-group operations do not mix the sublattice when the center is chosen to be atomic sites. (2) In the presence of sublattice indices the Green's functions

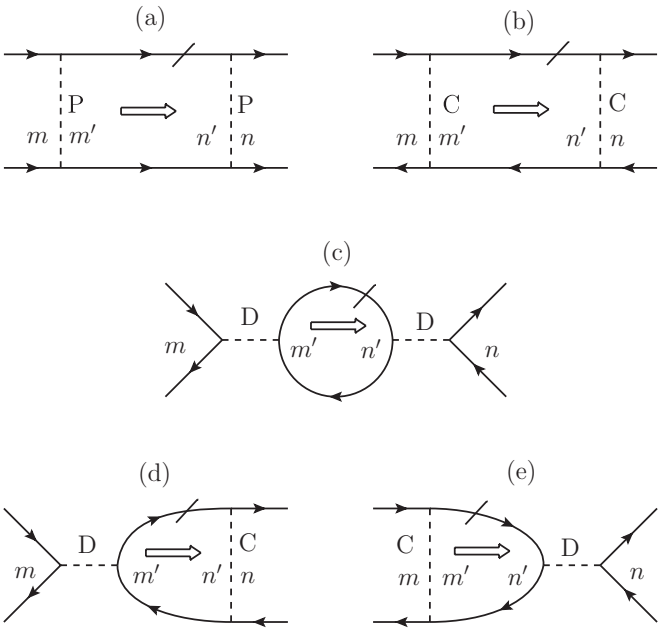

FIG. 7. One-loop diagrams contributing to the flow of the four-point vertex function in the pairing channel (a), crossing channel (b), and direct channel (c)–(e). Here $m,m'n,n'$ denote form factors, while the momentum and spin indices are left implicit. The open arrows indicate the flow of the collective momentum. The slashed lines are single-scale fermion propagators. The slash can be placed on either internal line associated with the loop.

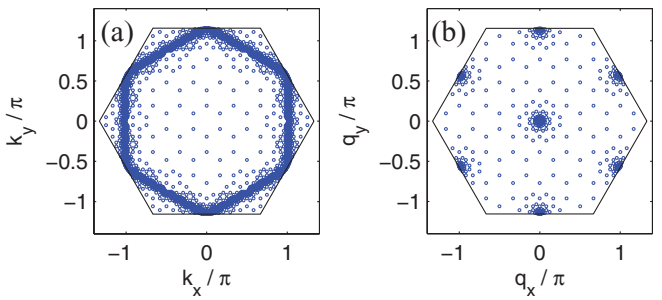

FIG. 8. (Color online) Examples of self-adaptive $\mathbf{k}$-mesh (a) and $\mathbf{q}$-mesh (b) used for loop integrations and collective momenta for interactions, respectively. Notice that in (a) the mesh is too dense near the Fermi surface to be differentiated by the naked eye.

are matrices. (3) In order to ensure that in momentum space P, C, and D transform exactly as a product of form factors, care must be taken in choosing the phase of the Bloch states for complex unit cells.

The pairing function is determined as follows. A singular mode ϕ^{α}_{sc} corresponds to a pairing operator $\sum_{m=(m,a)} c^{\dagger}_{a\uparrow}(\mathbf{k})\phi^{\alpha}_{sc}(m) f_m(\mathbf{k})^* c^{\dagger}_{a_m\downarrow}(-\mathbf{k})$ in the momentum space, where a_m is determined by $m = (m,a)$ (for all associated vectors $\mathbf{r}$). The parity of the pairing matrix function under space inversion determines automatically whether it is a spin singlet or spin triplet. A further unitary transform can be used to get the momentum space gap function.

In the current implementation of SM-FRG the sampling of momentum space ($\mathbf{k}$ and $\mathbf{q}$) is performed on self-adaptive meshes. As an example, Fig. 8(a) shows the $\mathbf{k}$ mesh, which is progressively denser in approaching the Fermi surface or van Hove points (if they are close to the Fermi level). This is important for our problem because of the rapid variation of the Fermi velocity near the van Hove singularities. The $\mathbf{k}$ mesh is obtained as follows. First define an energy scale Ω (of the order of the bandwidth), and begin with six equal-area triangles spanning the Brillouin zone. Break a specific triangle into four smaller equal-area ones if any eigenenergy $|\epsilon_{\mathbf{k}}| \leqslant \Omega$ in the original triangle. Then lower the energy scale as $\Omega \to \Omega/b$ ($b > 1$) and repeat the above process recursively. The centers of the triangles form the mesh points. Combining the triangle areas, they are used in the loop integrations in Eq. (A1). In our implementation, we perform the above processes eight to ten times, so that the last generation of triangles has a linear size of order $2^{-8}\pi$–$2^{-10}\pi$, and the center of such triangles are sufficiently close to (or accidentally on) the Fermi surface. The $\mathbf{q}$ mesh as in Fig. 8(b) used for the interactions includes all important scattering momenta: the origin and the high-symmetry nesting vectors. We devise a function $\eta_{\mathbf{q}}$ such that it is zero at those important scattering momenta, and generate the mesh in a similar fashion as for $\mathbf{k}$, except that Ω becomes an artificial scale and $\eta_{\mathbf{q}}$ is used in place of $\epsilon_{\mathbf{k}}$. A similar q mesh already appears in Ref. 14.

[1] K. S. Novoselov, A. K. Geim, S. V. Morozov, D. Jiang, Y. Zhang, S. V. Dubonos, I. V. Gregorieva, and A. A. Firsov, Science **306**, 666 (2004).

[2] For a review see A. H. Castro Neto, F. Guinea, N. M. R. Peres, K. S. Novoselov, and A. K. Geim, Rev. Mod. Phys. **81**, 109 (2009).

[3] X. Du, I. Skachko, F. Duerr, A. Luican, and E. Y. Andrei, Nature (London) **462**, 192 (2009).

[4] K. I. Bolotin, F. Ghahari, M. D. Shulman, H. L. Stormer, and P. Kim, Nature (London) **462**, 196 (2009).

[5] D. A. Siegel, Cheol-Hwan Park, C. Hwang, J. Deslippe, A. V. Fedorov, S. G. Louie, and A. Lanzara, Proc. Natl. Acad. Sci. (USA) **108**, 11365 (2011); D. C. Elias, R. V. Gorbachev, A. s. Mayorov, S. V. Morozov, A. A. Zhukov, P. Blake, L. A. Ponomarenko, I. V. Grigorieva, K. S. Novoselov, F. Guinea, and A. K. Geim, Nat. Phys. **7**, 701 (2011).

[6] A. L. Walter, A. Bostwick, K.-J. Jeon, F. Speck, M. Ostler, T. Seyller, L. Moreschini, Y. J. Chang, M. Polini, R. Asgari, A. H. MacDonald, K. Horn, and E. Rotenberg, Phys. Rev. B **84**, 085410 (2011).

[7] P. W. Anderson, Science **235**, 1196 (1987).

[8] S. Pathak, V. B. Shenoy, and G. Baskaran, Phys. Rev. B **81**, 085431 (2010).

[9] A. M. Black-Schaffer and S. Doniach, Phys. Rev. B **75**, 134512 (2007).

[10] J. González, Phys. Rev. B **78**, 205431 (2008); C. A. Lamas, D. C. Cabra, and N. Grandi, *ibid.* **80**, 075108 (2009); D. Makogon, R. van Gelderen, R. Roldán, and C. M. Smith, *ibid.* **84**, 125404 (2011).

[11] E. V. Castro, A. G. Grushin, B. Valenzuela, M. A. H. Vozmediano, A. Cortijo, and F. de Juan, Phys. Rev. Lett. **107**, 106402 (2011).

[12] R. Nandkishore, L. Levitov, and A. Chubukov, e-print arXiv:1107.1903 (to be published).

[13] Tao Li, e-print arXiv:1103.2420 (to be published).

[14] C. Husemann and M. Salmhofer, Phys. Rev. B **79**, 195125 (2009).

[15] H. Zhai, F. Wang, and D.-H. Lee, Phys. Rev. B **80**, 064517 (2009).

[16] C. Honerkamp, Phys. Rev. Lett. **100**, 146404 (2008).

[17] M. Salmhofer and C. Honerkamp, Prog. Theor. Phys. **105**, 1 (2001).

[18] C. Honerkamp, M. Salmhofer, N. Furukawa, and T. M. Rice, Phys. Rev. B **63**, 035109 (2001).

[19] F. Wang, H. Zhai, Y. Ran, A. Vishwanath, and D.-H. Lee, Phys. Rev. Lett. **102**, 047005 (2009).

[20] We note that by setting $l = 1$ above does not produce independent spatial form factors because the above three form factors are complete for the three first neighbor bonds. Hence by using $f_{d_1,d_{1'}}$ we are able to investigate, e.g., both p- and d-wave pairing (of course their total form factors have completely different spin and sublattice structures).

[21] Translating P, C, and D back to Γ_{1234}, the divergence criterion is smaller since two form factors must be accounted for.

[22] Fan Yang, Hui Zhai, Fa Wang, and Dung-Hai Lee, Phys. Rev. B **83**, 134502 (2011).

[23] M. Kiesel, C. Platt, W. Hanke, D. A. Abanin, and R. Thomale, e-print arXiv:1109.2953. In this paper the electron filling f is defined as the number of electrons per site per spin, which is related to our doping level as $\delta = 2f - 1$.

[24] C. Karrasch, R. Hedden, R. Peters, Th. Pruschke, K. Schönhammer, and V. Meden, J. Phys.: Condens. Matter **20**, 345205 (2008).